Chapter 6

Results: Pulsed magnetic focusing

"You cannot depend on your eyes when your imagination is out of focus."
Mark Twain

The $\mathcal{ABCD}$ matrix formalism outlined in the previous chapter is a useful starting point for studying pulsed magnetic focusing. However, this formalism ignores magnetic aberrations arising due to the departure of the real potential from an ideal parabolic spatial dependence (see Figure 4.6). The attributes of parabolic lenses are unimportant, unless it can be shown that experimentally realistic lenses are sufficiently parabolic for such an approximation to be appropriate. For a non-parabolic potential the change in position and velocity which occur during lensing must be calculated numerically. In this chapter the 'perfect' atomic lens approximations are tested by performing numerical focusing simulations. Work contained within this chapter has led to the publication of refs. [141, 145, 146] and has been done in collaboration with the other authors.

6.1 Methodology

The approach adopted was a numerical simulation, in which the trajectories of typically 5,000 atoms are followed. The cloud and its motion are treated classically, and for the atomic densities encountered in the expanding cloud,

the collision rate is negligible. The atoms travel on ballistic trajectories, except when a magnetic impulse is applied, in which case the full Stern-Gerlach force is included in the numerical integration. The effects of gravity were included, but these effects on the quality of focus were found to be negligible for the parameters used in these simulations.

As in previous chapters, a specific experimental setup described in Section 3.2 is modelled. Initially the focusing is studied without the presence of a laser guide however, and for those simulations a slightly larger MOT size is used ($\sigma_R = 0.4$ mm). In all the simulations the maximum current value in any coil was limited to $NI = 10,000$ Amps. Two measures of the focused cloud size are used and these are outlined below.

6.1.1 Root mean square cloud radius

Useful statistical parameters for describing the evolution of a Gaussian atomic cloud are the time-dependent axial (σ_z) and radial (σ_z) rms cloud radii (the standard deviations), as well as their aspect ratio $\xi = \sigma_z/\sigma_r$. A measure of the harmonicity of a lens can be given by comparing the expected harmonic focus size to the rms radii of the simulated atom cloud at the time of the harmonic focus. The important drawback of this rms approach is that the final location of atoms after a magnetic lens is highly nonlinear with respect to initial conditions. An atom with a velocity in the wings of the initial Gaussian distribution will experience highly anharmonic lensing, as it will be far from the centre of the lens during the magnetic impulse. Thus a few atoms can completely alter the rms width of the cloud.

6.1.2 Atoms in the harmonic region

Another method to quantify the focus is to monitor the fraction of the atoms entering the focus region of a purely harmonic lens. The initial radial and axial cloud standard deviations are σ_R, so the final standard deviations for a harmonic lens are $\sigma_r = \mathcal{A}_r\sigma_R$ and $\sigma_z = \mathcal{A}_z\sigma_R$. By renormalising the dimensions so that the radial and axial dimensions are measured in terms of these final

focus standard deviations, then a sphere with radius $R_0 = 1.53817$ defined by:

$$\frac{\int_0^{R_0} r^2 e^{-\frac{r^2}{2}} dr}{\int_0^{\infty} r^2 e^{-\frac{r^2}{2}} dr} = \frac{1}{2}\,, \tag{6.1}$$

will contain half of the atoms of the focused Gaussian distribution. This renormalisation process is illustrated in Figure 6.1.

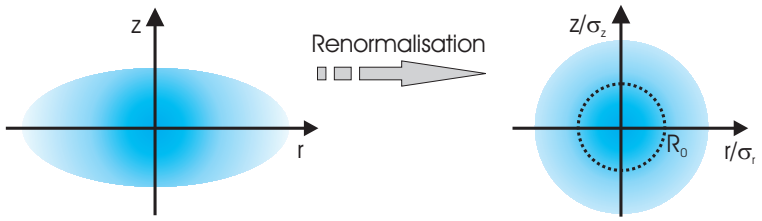

Figure 6.1: The diagram shows how a atomic cloud's dimensions are renormalised by dividing the distances by the final harmonic lens standard deviations. For a harmonic lens the dotted region contains half the atoms.

For numerical simulations the fraction of atoms entering this harmonic focus is measured, and multiplied by twice the relative density increase of a purely harmonic lens (i.e. $2\mathcal{A}_r{}^{-2}\mathcal{A}_z{}^{-1}$) to get a measure of the relative density increase afforded by a real lens. Note that the centre of the harmonic focus region is the final position of an atom initially in the centre of the Gaussian position and velocity distributions. This will lead to a slight underestimation in the density increase (it has been assumed the mean cloud position follows the initial centre-of-mass).

6.2 Single-impulse magnetic focusing

6.2.1 Strategy I: axial defocusing/radial focusing

The simplest implementation of pulsed magnetic focusing is using a single current carrying coil (Strategy I). The trajectories of atoms subject to such a lens are shown in Figure 6.2. The radial direction is focused whereas the axial direction is defocused due to the opposite sign of the magnetic field curvature. Although the lens system is symmetrical, the atom trajectories in the focused radial direction are asymmetrical, which is evidence of lens aberrations.

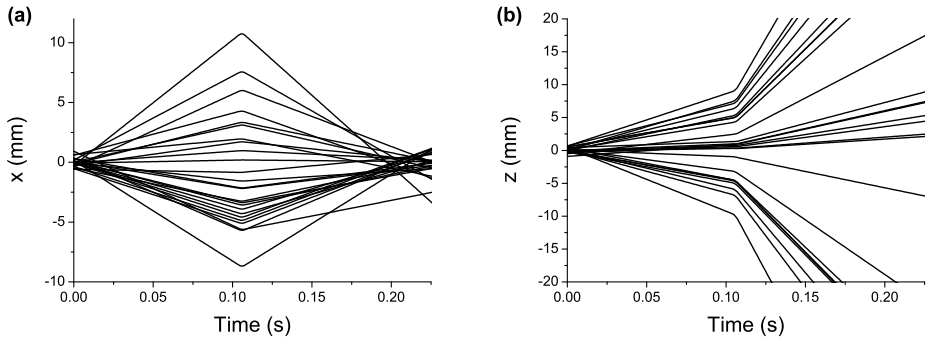

Figure 6.2: The trajectories of 25 atoms subject to a 5 cm Strategy I lens being pulsed on at $\lambda = 0.5$. Plot (a) shows radial distance and (b) shows the axial distance plotted against time.

Figure 6.3 (a) shows the evolution of σ_x for a launched cloud of 500 atoms subject to a radially converging lens constructed from a single coil. The impulse is applied half-way in time, and the length of the impulse is chosen to reverse the transverse velocity, as can be seen from the change in sign of the gradient after $t = 106\,\text{ms}$. For this case, the $\mathcal{ABCD}$ matrix predicts a radial focus with magnification -1, which is in excellent agreement with the numerical simulation using a parabolic lens (using the strength of eqn. (4.16)). The vertical line at $t = 212\,\text{ms}$ corresponds to the imaging time. For real coils, it is seen that the focused cloud image is significantly larger than the initial cloud. The aberration worsens as the coil radius decreases.

Figure 6.3 (b) contains an analysis of the cloud in terms of shells of different radii measured from the centre of the coil; atoms further from the centre are not focused as tightly, and also focus earlier in time. As the ratio between cloud

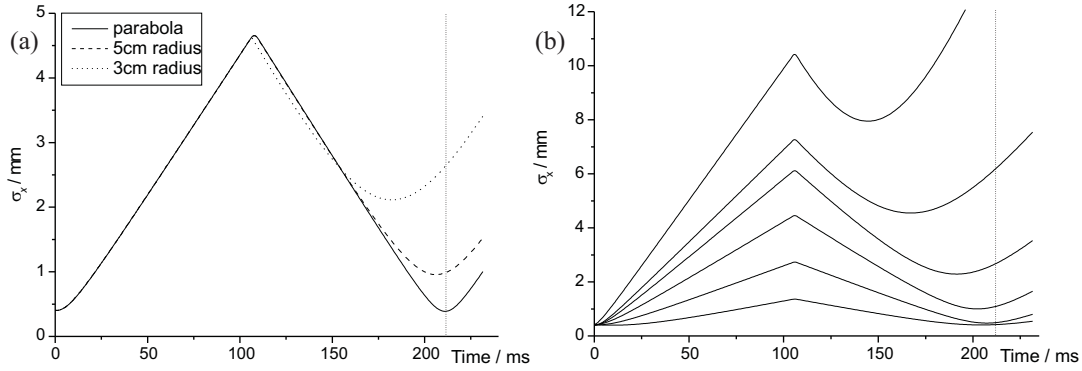

Figure 6.3: (a) Simulation of 500 atoms going through a Strategy I lens ($NI = 10,000$ Amps). The solid, dashed and dotted lines correspond to a parabolic approximation lens, a 5 cm radius lens, and a 3 cm radius lens respectively. The duration and timing of the impulse is chosen using the $\mathcal{ABCD}$ matrix formalism, bringing the atoms to a focus 22 cm above their launch height. (b) A shell plot of 1,000 simulated atoms passing through a 3 cm radius Strategy I lens. The distances from the coil centre are 0-10% of the coil radius, 10-20%, through to 50-60%. Atoms further from the centre are not focused as well, and the focusing occurs at earlier times. Both of these factors degrade the image quality and size.

extent and coil radius decreases, the departure of the field from the parabolic approximation becomes less significant. Therefore one method to reduce the aberrations experienced by the atoms is to increase the coil radius, or decrease the atomic cloud temperature.

Figure 6.4 (a) plots the change in radial cloud size at the predicted focus, σ_x/σ_{x_i}, against coil radius. The optimum coil radius for a Strategy I lens carrying $NI = 10,000$ Amps is 8 cm. The coil radius cannot be increased indefinitely, as even though the lens' harmonicity at the centre will be improved, the pulse duration will also increase; see Figure 6.4 (b). There is both an experimental and theoretical limit to how long the pulse duration can be. The experimental limit is due to long pulse durations causing potentially catastrophic heating in the coil circuit. The theoretical limit is due to the atoms experiencing more of the off-centre lens aberrations, including time-varying lens frequencies, as they move through the lens. The longer the pulse duration, the larger these effects will be.

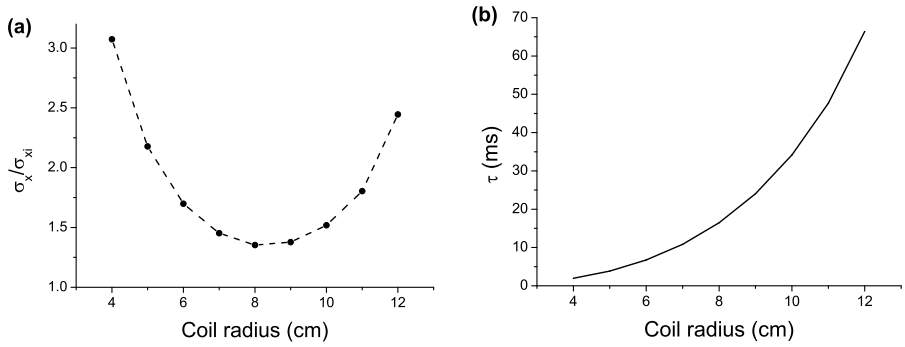

Figure 6.4: (a) The change in radial cloud size, σ_x/σ_{x_i}, at the predicted focus ($T = 212$ ms) is plotted against coil radius for a Strategy I lens ($NI = 10,000$ Amps). (b) The pulse duration, τ, is plotted against coil radius.

6.2.2 Strategies II-III: axial/radial focusing

Another method to reduce performance limiting aberrations is to use an optimised double-coil lens (Strategies II and III). Attention is turned to obtaining the minimum cloud size by investigating the effect of varying the λ parameter, and in the process it will be shown that double-coil lenses out perform their single-coil counterparts. As discussed in Section 5.2, a thin parabolic lens produces the smallest cloud size when $\lambda \to 1$, i.e. the pulse is applied as late in time as possible. This is a manifestation of Liouville's theorem - a more compact spatial extent can be generated at the expense of a larger velocity spread.

Figure 6.5 shows simulations of radial focusing. The radial cloud expansion factor, σ_x/σ_{x_i}, is plotted as a function of the imaging parameter λ. It can be seen that the smallest cloud size for a parabolic lens (solid line) occurs when one waits as long as possible before focusing, i.e. λ is as close as possible to 1 (limited by the maximum value given by eqn. (5.13)).

The figure also shows how well Strategy I and II lens approximate a parabolic lens. When $\lambda > 0.3$ a 5 cm single-coil lens diverges from the parabolic case and a double-coil starts to diverge when $\lambda > 0.5$. The plot clearly shows that the double-coil produces a lens that better approximates the ideal case. For experimentally-realistic parameters it is seen that it is possible to achieve a final radial cloud size that is smaller than the initial size. At $\lambda = 0.6$ the radial extent of the final cloud is 0.8 times the original radial extent of the cloud.

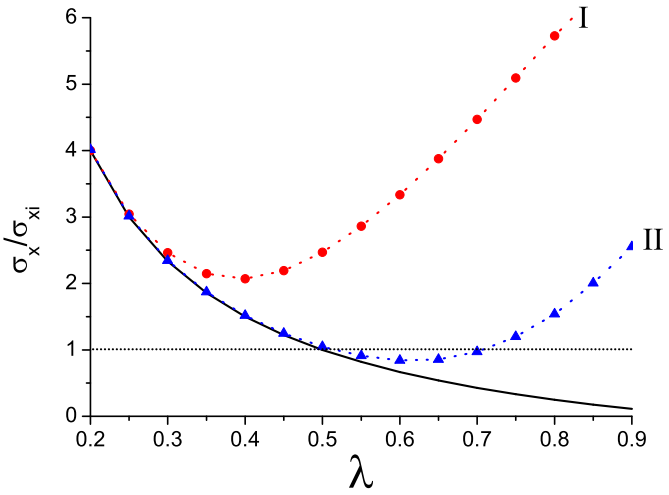

Figure 6.5: The radial expansion factor, at $T = 212\,\text{ms}$, for 5 cm radially converging lenses is plotted against λ. The solid line without symbols shows the parabolic lens solution and the dotted lines with red circles (blue triangles) show the result of atoms passing through a Strategy I (II) lens.

Like its double-coil partner, Strategy III produces an axially converging/radially diverging lens with a high level of harmonicity comparable to that of Strategy II.

Compared to the $\mathcal{ABCD}$ matrix result there is a marked difference in the behaviour of the minimum radially-focused cloud-size for fields from real coils – the value of λ at which the $\mathcal{ABCD}$ minimum is obtained is dominated by aberrations in the magnetic field. The $\mathcal{ABCD}$ matrix approach does not provide an adequate description of pulsed magnetic focusing when one considers the entire atomic cloud.

The easiest way to reduce aberrations further appears to be the use of a very large coil radius. Unfortunately the curvature of the field decreases with the cube of the coil radius (eqn. (4.17)), which necessitates longer pulse durations for larger radius coils. This increase in pulse duration reduces the maximum value of λ that can be used and therefore also limits the minimum cloud size. The aberrations can only be further reduced by increasing the current-turns, something which has experimental limitations.

6.2.3 Strategies IV-VI: isotropic 3D focusing

Isotropic 3D focusing can be achieved using two coils with differing currents (Strategy IV). For realistic experimental parameters, the numerical simulations showed that the aberrations in the lens smeared out any focusing. However, for unrealistically large lens radii and large currents (e.g. 15 cm and 200, 000 Amp-turns) it is possible to achieve 3D focusing.

As discussed in Section 4.4.4, a single coil can be made to have isotropic curvature (Strategy V). At $z = \pm\sqrt{2/7}a$, the axial and radial curvatures are equal, and the gradient of the field is non-zero. A numerical simulation was performed for a launched cloud, with an impulse applied when the cloud's centre of mass reached a distance $z = +\sqrt{2/7}a$ from the centre of a single coil. Due to the large departure from harmonicity for the experimentally realistic parameters used, aberrations dominated and focusing was not observed.

The baseball lens (Strategy VI) yields the best isotropic 3D lens. Figure 6.6 shows the temporal evolution of the volume expansion factor, $(\sigma_x\sigma_y\sigma_z/\sigma_{x_i}\sigma_{y_i}\sigma_{z_i})$, for a launched cloud subject to a focusing pulse from a baseball lens. Five different values of λ are depicted, from 0.3 to 0.7 in steps of 0.1. The bias coils have radii of $a = 4\,\text{cm}$, separation $S = 1$, and current $NI = 1,541\,\text{A}$; the baseball has sides of length $W = L = 2$ and current $I' = 10,000\,\text{A}$. These values lead to an angular frequency $\omega = 63\,\text{rad/s}$ in all directions. The minimum cloud size is obtained when $\lambda = 0.3$. At the focal time, $T = 212\,\text{ms}$, the volume has increased by a factor of 50. This is to be contrasted with the 13, 000 increase in cloud volume if no magnetic lens was used.

In Figure 6.7 the relative density increase after the baseball lens is plotted in terms of the timing parameter λ. The red dots correspond to the relative density increase using rms widths for the volume. The blue dots show the relative density increase as the fraction of atoms in the harmonic focus zone times twice the harmonic density increase, see Section 6.1.2. It is clear that very different conclusions are reached based on whether the rms radius of the focused atomic cloud, or the fraction of atoms which reach the harmonic focus are considered.

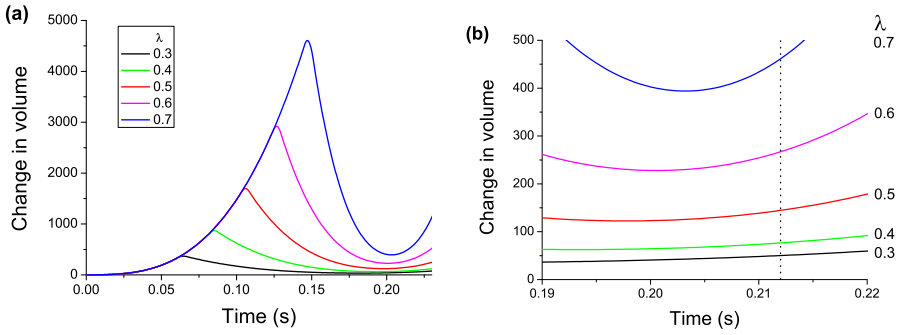

Figure 6.6: (a) A simulation of 1,000 atoms sent through a 4 cm isotropic baseball coil lens (Strategy VI). The ratio of the cloud volume to the initial volume ($\sigma_x\sigma_y\sigma_z/\sigma_{x_i}\sigma_{y_i}\sigma_{z_i}$) is plotted as a function of time for values of λ ranging from 0.3 to 0.7. (b) A close-up of the simulations near the $t = T$ imaging time (vertical line).

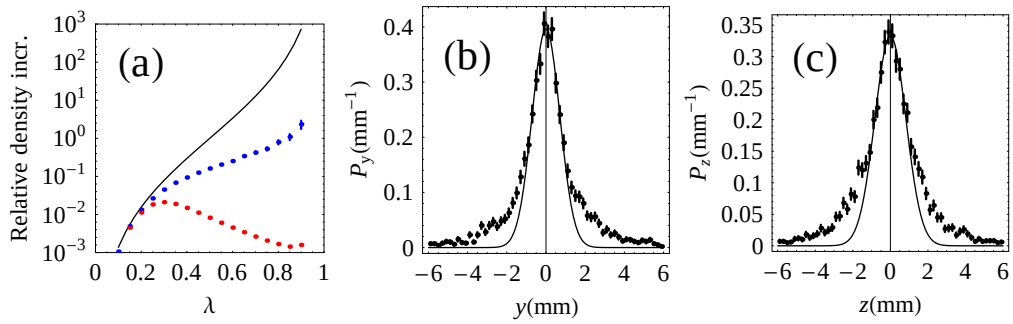

Figure 6.7: Image (a) shows the relative density increase (with error bars, for a 5,000 atom simulation) based on: a purely harmonic lens (black curve), the fraction of atoms in a real lens arriving at the harmonic focus region (blue dots), the ratio of rms cloud volume before and after a real lens (red dots). Images (b) and (c) show the spatial probability distributions at the focus (black dots) in the y and z directions, respectively, where the non-Gaussian wings of the distribution can be clearly seen. These two distributions are taken from the $\lambda = 0.5$ lens simulation, in which case 16% of the atoms are in the harmonic focus region. The Gaussian fits in (b) and (c) (as well as the x distribution) have an area of $\approx 70\%$. [Figure generated in collaboration with A. S. Arnold.]

By only looking at rms widths the optimum lens position occurs at $\lambda = 0.3$, corresponding to a factor of 50 decrease in density. However considering the fraction of atoms in the harmonic focus zone times the harmonic density increase, the optimum position is now $\lambda = 0.9$. The relative density increase is 2.3, which corresponds to 0.3% of the cloud focused to a density 729 times greater than it was originally. The source of this discrepancy between methods can be seen in Figure 6.7 (b-c) where the non-Gaussian wings produce an

over estimate of the rms cloud width. The y and z standard deviations for the Gaussian fits (black curves) are 730 μm and 820 μm respectively; an almost isotropic distribution.

It is interesting to note that for the parameters simulated, the results of a 'pure' Ioffe-Pritchard lens ($W = 2$, $L \to \infty$ and $S = 2$) are almost identical to the baseball coil. Surprisingly the baseball lens performs better, and produces smaller cloud sizes at the focus. Within the last year, an experiment using the baseball lens described above has been used to isotropically focus Rb atoms; see refs. [158, 159] for more details.

6.3 Magnetic focusing and laser guiding

This section will investigate the axial focusing of an atomic cloud being guided within a 19 W laser beam with a beam waist of 250 μm. Four different lens designs presented in Chapter 4 will be investigated: the special case of Strategy IV that only has axial curvature ($\pm\mathbf{a}_0$); a Strategy II lens that can axially focus strong-field seeking (SFS) atoms; a Strategy III lens that can axially focus weak-field seeking (WFS) atoms. The properties of a 5 cm radius lens are tabulated in Table 6.1 for the four different designs studied. It is interesting to contrast the radial angular frequency of the lens with that of the laser guide. From eqn. (3.5) and the laser parameters above, the laser angular frequency is $\omega_{r_L} = 435$ rad/s. Therefore in the radial direction the laser will dominate over the magnetic field's influence.

	S	NI_1 (A)	NI_2 (A)	a_0 (m/s^2)	ω_r (rad/s)	ω_z (rad/s)	τ (ms)
Axial-only	$\sqrt{3}$	-1,429	10,000	+121	0	49	11.6
lenses	$\sqrt{3}$	10,000	-1,429	-121	0	49	6.6
Strategy II lens	0.58	10,000	10,000	0	70i	100	1.9
Strategy III lens	2.63	10,000	10,000	0	42i	59	5.5

Table 6.1: The focusing properties are tabulated for the 5 cm magnetic lenses used in conjunction with the laser guide. The pulse duration has been calculated for a pulse occurring at $\lambda = 0.5$. The accelerating and decelerating axial-only lenses from Section 4.4.3 are shown in rows 1 and 2. The Strategy II (SFS) and Strategy III (WFS) lenses from Section 4.4.2 are shown in rows 3 and 4. A complex angular frequency corresponds to negative curvature and hence defocusing.

6.3.1 Strategy IV: axial-only focusing

The use of a lens that does not perturb the radial motion would seem an ideal candidate for combining with a laser guide. In Figure 6.8 the combined laser and the full magnetic field potential using elliptic integrals has been plotted. The constant B_1 term, arising from the lens' axial asymmetry, has been subtracted to emphasise the axial curvature and lack of radial curvature.

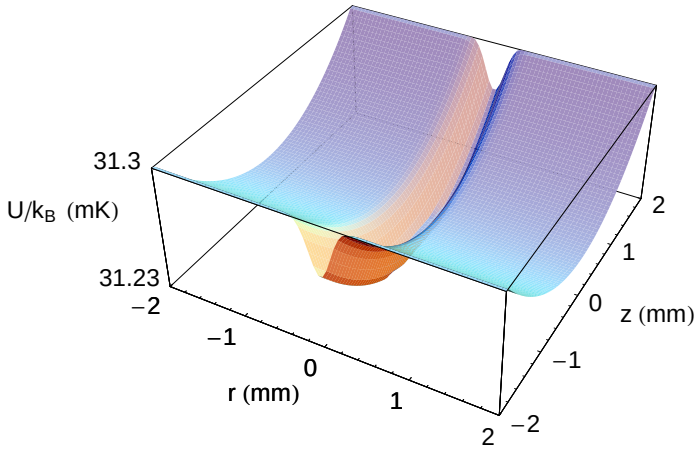

Figure 6.8: The potential energy surface of the combined laser and axial-only magnetic lens. The lens has a radius of 5 cm and carries a maximum current of $NI = 10,000$ Amps. The B_1 term has been subtracted to show the focusing properties of the lens.

The quality of the focus was investigated, and Figure 6.9 plots the change in axial standard deviation, σ_z/σ_{z_i}, against time for different values of λ. There is no $\lambda = 0.7$ line for the decelerating lens due to the reason explained in Section 5.2.1. The lens timings and launch velocity were chosen so that the cloud's apex had a height of 22 cm. Neither lens causes atoms to be lost from the laser guide as a result of the magnetic pulse. For both decelerating and accelerating 5 cm lenses the minimum cloud size is achieved for $\lambda = 0.5$, resulting in a change in axial standard deviation of 1.18 and 1.64 respectively. If the lenses were free of aberrations, one would expect to see no change in axial size at the focus (i.e. $\sigma_z/\sigma_{z_i} = 1$). An unfocused cloud's axial size would have increased by a factor of 34 and 59 respectively. The aberrations of the axial-only lens inhibit achieving a compressed image and also cause the focusing to occur ~ 10 ms after the predicted focal times. The focusing performance in contrast with the 1D focusing of Section 6.2.2 is significantly worse.

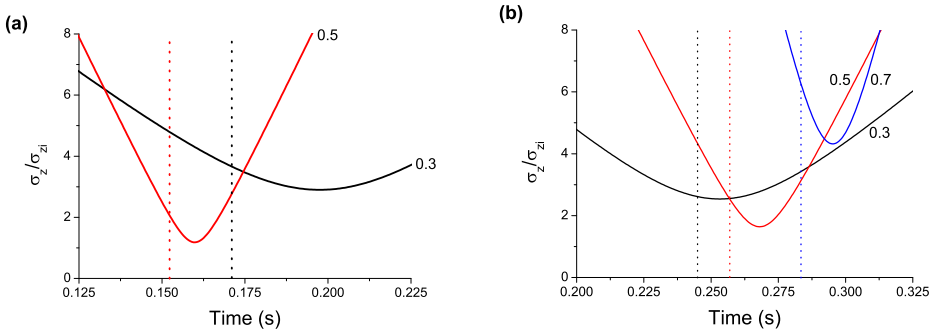

Figure 6.9: The change in axial cloud standard deviation, σ_z/σ_{z_i}, is plotted against time for (a) a decelerating and (b) an accelerating 5 cm radius axial-only lens. Three lens positions are plotted: $\lambda = 0.3$ (black line), 0.5 (red line) and 0.7 (blue). The radial confinement was provided by a 19 W laser guide with a beam waist of 250 μm. The vertical lines indicate the predicted focus times - the colours matching the corresponding line.

6.3.2 Strategies II-III: axial/radial focusing

The effect of significant aberrations and the complication of the constant acceleration for axial-only lenses are undesired. These can be avoided by using either the Strategy II or Strategy III lenses described in Section 4.4.2. The drawback with such lenses is that the radial direction is now also perturbed. The choice of which lens to use depends on whether the atoms are strong-field or weak-field seeking, namely Strategy II and III respectively. The combined potential resulting from the magnetic and laser fields is shown in Figure 6.10 (a) for a Strategy III lens. At the centre, the optical dipole potential dominates and there is positive curvature causing focusing in all three spatial directions. However, away from the z-axis the magnetic potential becomes significant and the radial curvature turns negative. This turn over is shown more clearly in the $z = 0$ cross section in Figure 6.10 (b). The trap depth has been reduced, which means some atoms will have become energetically unbound during the lens pulse, see eqn. (3.6).

In Figure 6.11 the trajectories of 25 atoms are plotted in the centre of mass frame for (a) the radial direction and (b) the axial direction. In this example a 5 cm Strategy III lens was positioned at $\lambda = 0.5$ and was pulsed on for 5.5 ms to bring the cloud to a focus at the fountain apex. In this simulation two atoms were lost as a result of the magnetic lens pulse. Before investigating the quality of the focused cloud, attention is turned to characterising these pulse losses.

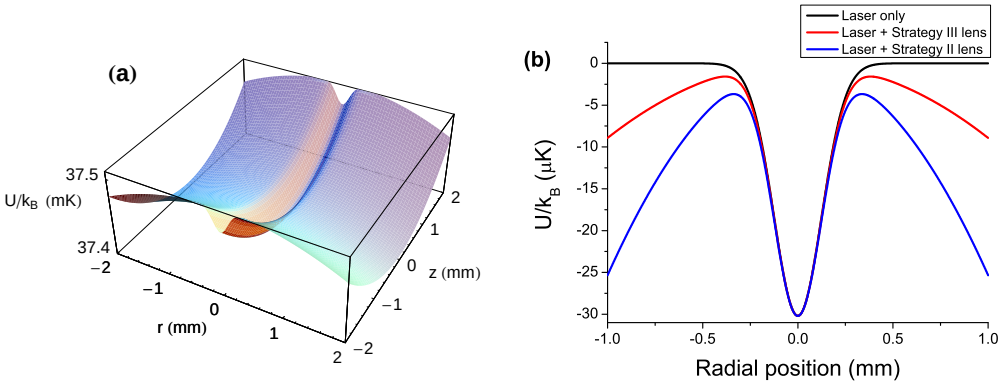

Figure 6.10: Plot (a): The potential energy surface of the combined laser and magnetic fields for a Strategy III lens is plotted against radial and axial position. The 19 W laser has a beam waist of 250 μm. The lens has a radius of 5 cm and has $NI = 10,000$ Amps in the coils. In (b) the cross section along the $z = 0$ line is plotted. The black line is the laser only potential, the blue line is the combined laser and magnetic potential for a Strategy II lens and the red line is the combined potential for a Strategy III lens. For a Strategy II (Strategy III) lens the trap depth is 88% (95%) of the laser depth. Note: the combined potentials have offsets added so that the three minima coincide.

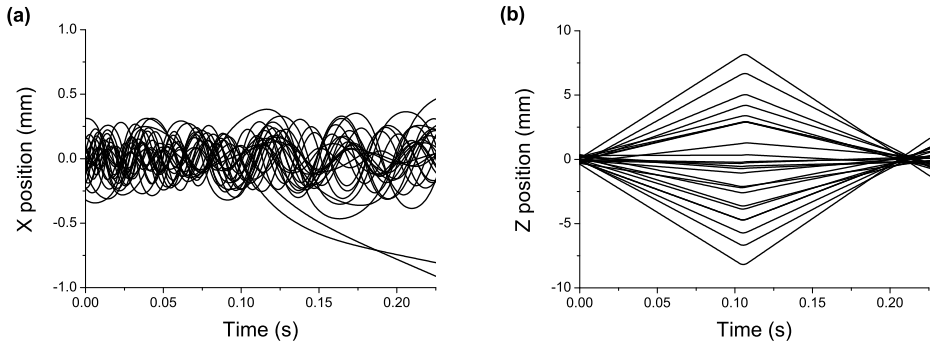

Figure 6.11: The trajectories of 25 WFS atoms are simulated passing through the laser guide and being focused by a 5 cm radius Strategy III lens. The pulse occurs at $\lambda = 0.5$ and has a duration of 5.5 ms. Plot (a) shows the x-axis position and plot (b) the z-axis position relative to the cloud's centre of mass.

If an atom's velocity was not modified, the 'window of opportunity' to escape only lasts as long as the pulse time, which is usually of the order of a few milliseconds. This escape time is short compared to the radial oscillation period within the laser guide. The period is obtained from eqn. (3.5): $T_{\rm osc} = 2\pi/\omega_{r_{\rm L}}$. For a 19 W laser with $1/e^2$ radius of 250 μm this corresponds to a period of 14 ms. Therefore an individual atom will only perform $\sim 1/10^{\rm th}$ of an oscillation and is unlikely to escape. One would expect the loss due to this mechanism to scale with the pulse duration τ.

However, the magnetic pulse modifies the velocity of the atoms. For some atoms this can result in them becoming energetically unbound both during and after the pulse. Over time these unbound atoms will escape from the guide. The immediate change in bound fraction and its subsequent effect on the guided atoms are illustrated in Figures 6.12 (a) and (b) respectively. The initial overshoot in the bound fraction demonstrates the losses due to a lowered potential described above. The momentum kick an atom receives for a given λ is independent of the lens design. Therefore one would expect to find that the lens design has a negligible effect on the loss due to the pulse; this is verified by comparing the red and blue lines in Figure 6.12. The loss due to the magnetic pulse is $\sim 2\%$, and is tiny compared with the loss associated with the initial loading of the laser guide.

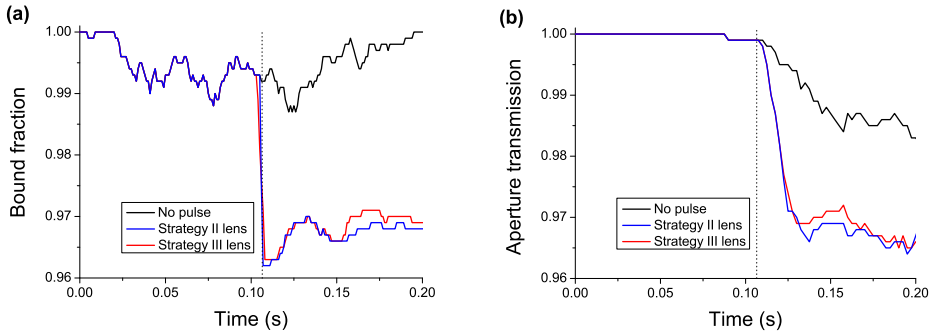

Figure 6.12: Plot (a) shows the evolution of the ratio of bound atoms to the initial number of bound atoms. Three cases are plotted: no magnetic pulse (black line), a Strategy II lens for SFS atoms (blue line) and a Strategy III lens for WFS atoms (red line). The lens pulse occurs at $\lambda = 0.5$. Plot (b) is identical to (a) except for the y-axis now represents the atom transmission through a 0.5 mm radius aperture. Only atoms that were initially bound were considered when calculating the transmission. Both Strategy II and Strategy III lines trace each other remarkably well which is an indication that pulse loss is independent of the lens design. The simulation was performed with 5,000 atoms.

Attention is now returned to studying the focusing properties of the magnetic lenses. For small radius lenses, aberrations tend to dominate resulting in a poor focus and unpredictable focus time. When the lens radius is increased above 7 cm for a Strategy II lens and above 5 cm for a Strategy III lens, no further improvements are observed. The Strategy II lens suffers from worse aberrations as the atoms experience more of the anharmonic B-field due to their closer proximity to the coils.

In Figure 6.13 the change in axial standard deviation, σ_z/σ_{z_i}, for a 5 cm Strategy III lens is plotted against time for different values of λ. The effect of aberrations is significantly less for this design compared with an axial-only lens (Figure 6.9). The minima occur within ~ 3 ms of the predicted focal time and are only slightly worse than values achievable with an aberration-free lens. For the case of $\lambda = 0.7$ the cloud is compressed along the axial direction to half of its initial size. Unlike Section 6.2.2 where aberrations dominate a similar plot at high λ, one finds that for laser guided atoms this is not the case. This is due to the strong radial confinement provided by the laser guide.

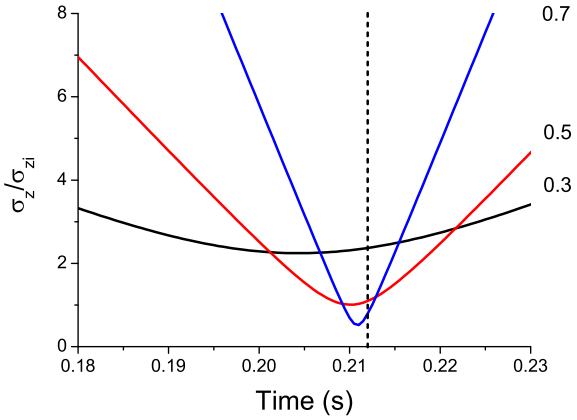

Figure 6.13: The change in the cloud's axial standard deviation, σ_z/σ_{z_i}, is plotted against time for a Strategy III lens. Three lens positions are plotted: $\lambda = 0.3$ (black line), 0.5 (red line) and 0.7 (blue), the minimum change is 2.2, 1.0 and 0.5 respectively. The expected minima based upon the magnification $(\lambda - 1)/\lambda$ are 2.33, 1.00 and 0.43 respectively. The dashed vertical line indicates the predicted focal time of 212 ms.

6.3.3 Transported cloud properties

Numerical simulations were performed to compare the four hybrid transportation schemes. The position and velocity standard deviations of the atomic cloud were computed after tracing the trajectories of individual atoms. The results are presented in Table 6.2. For ease of comparison the equivalent temperature, $\mathcal{T}$, corresponding to a given velocity and the cloud aspect ratio, $\xi = \sigma_z/\sigma_r$, are also tabulated. It should be noted that when the cloud is trapped in the upper chamber, the temperature will rethermalise via collisions. The trap geometry will determine the rethermalised temperature.

	MOT	Bound atoms	Apex	$-a_0$ axial only lens	$+a_0$ axial only lens	Strategy II lens	Strategy III lens
σ_x (mm)	0.20	0.11	0.19	0.19	0.19	0.22	0.21
σ_z (mm)	0.20	0.20	9.4	0.37	0.66	0.22	0.21
$\xi = \sigma_z/\sigma_r$	1.00	1.81	50	1.96	3.57	1.03	0.99
σ_{vx} (cm/s)	4.42	2.53	1.67	1.63	1.68	1.71	1.71
σ_{vz} (cm/s)	4.42	4.41	4.40	3.93	4.03	4.42	4.47
$\mathcal{T}_x$ (μK)	20	7	3	3	3	3	3
$\mathcal{T}_z$ (μK)	20	20	20	16	17	20	20

Table 6.2: The table records the change in the atomic cloud's properties (position standard deviation σ, aspect ratio ξ, velocity standard deviation σ_v and temperature $\mathcal{T}$) for different transportation schemes. The columns are as follows: the initial cloud properties generated in the MOT; the cloud loaded from the MOT into a 250 μm beam waist laser guide; a cloud that has been transported within the laser guide to the 22 cm apex; a guided cloud that has been focused by a decelerating axial-only lens; a guided cloud that has been focused by an accelerating axial-only lens; a guided cloud that has been axially focused by a Strategy II lens; a guided cloud that has been axially focused by a Strategy III lens. Each lens has a radius of 5 cm, a maximum current of $NI = 10,000$ Amps and is pulsed on at $\lambda = 0.5$, see Table 6.1.

The first column of the table shows the properties of the initial MOT. The second gives the properties of atoms that are loaded into the guide. As expected these have a smaller radial extent, and as only the least energetic are loaded, a lower radial temperature. For the launched atoms with only laser guiding (third column) there is a slight increase in the radial size as a consequence of the laser beam diffracting, and the axial size grows by more than an order of magnitude. The cloud has a very elongated sausage shape ($\xi >> 1$). Focusing the laser guided cloud with either a decelerating or an accelerating axial-only lens (columns four and five respectively) produces a radial extent similar to an unfocused laser guided cloud, however the axial extent is significantly smaller than with no magnetic lens, but not as compact as the original launched cloud. This is a consequence of the aberrations associated with this lens design. The last two columns characterise the performance of optimised Strategy II and Strategy III lenses. Although there is a slight atom loss during the impulse associated with the negative radial curvature, the performance of these lenses is far superior, yielding moderately larger radial clouds, and one-to-one axial imaging. In all cases the slight increase of the radial extent is accompanied by a concomitant reduction of the radial temperature, a manifestation of Liouville's theorem.

Whilst initially it appears as if axial-only lenses would complement the radial laser guiding, the results of the simulations shows that the best strategy would be to use optimised harmonic lenses. The axial-only lens is harder to realise experimentally, and, as a consequence of the broken axial symmetry, has more significant aberrations. However, it can be used without further atom loss during the magnetic impulse. By contrast the optimised harmonic lenses do suffer a slight atom loss during the pulse. However this is insignificant compared to the initial loading loss. The axial-focusing of these two lenses is superior, and the simulations show that for realistic experimental parameters better than one-to-one axial focusing can be achieved when $\lambda > 0.5$.

There is a slight broadening of the cloud radially, arising from the laser beam's increased width. It might be possible to circumvent this by 'zooming' a lens such that the centre of mass of the atom cloud is always confined by the tightest focus of the beam. This would keep the initial cloud confined to the same final radial width. However this would be at the expense of significant experimental complexity.

6.4 Double-impulse magnetic focusing

This section compares the alternate-gradient numerical simulations with the purely harmonic lens calculations in Section 5.3. The (τ_1, τ_2) sample co-ordinates illustrated in Figures 5.5 (b) and (c) are used, in order to run numerical simulations for the relative density increases illustrated in Figure 6.14. The simulation has not (cf. Figure 6.7) used the rms volume of the cloud to represent the relative density increases as these result in extremely low relative density increases (typically 10^{-5} in (a) and 10^{-3} in (b)) that would reduce the figure's contrast.

For both strategies the numerical simulations trace the shape of the analytical relative density increase although aberrations result in reduced increases. The maximum relative density increases in (a) and (b) are 186 and 50 respectively. This is a marked improvement on the single-impulse focusing, however the cloud distribution is no longer isotropic. The harmonic focus aspect ratio has a range $12 \leq \xi \leq 17$ in (a) and $0.074 \leq \xi \leq 0.095$ in (b).

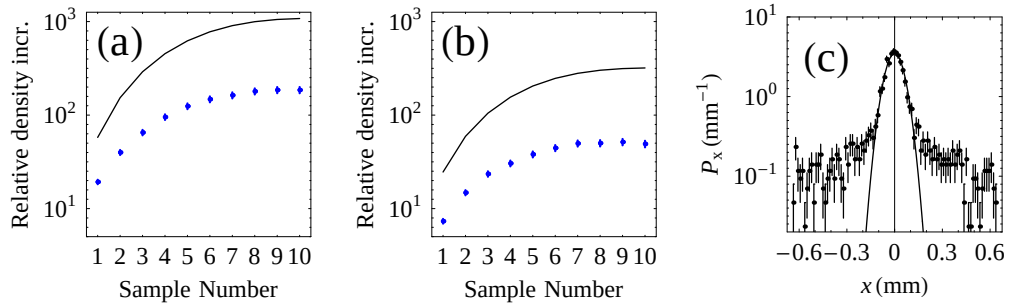

Figure 6.14: Images (a) and (b) use the (τ_1, τ_2) co-ordinates illustrated in Figure 5.5 (b) and (c) to show the relative density increase for alternate-gradient lensing Strategies AR and RA, respectively. There were 1,000 atoms in the simulation and relative density increases are shown for a pure harmonic lens (black curve), as well as the relative density increase for the fraction of atoms in a realistic lens arriving at the harmonic focus region (blue dots with error bars). In image (c) the strong spatial bimodal nature of the x focus for the leftmost point in (a) is clearly seen on a log scale. The Gaussian fit (with $\sigma_x = 56\,\mu$m) contains 49% of the 3,000 simulated atoms used in (c). [Figure generated in collaboration with A. S. Arnold.]

In certain applications, for example microtrap loading and lithography, the sausage-shaped distribution ($\xi > 1$) with its reduced radial spread could be beneficial. Figure 6.14 (c) plots the distribution of a cloud focused via Strategy AR. The standard deviations for the Gaussian fits to the core of the x, y, and z distributions are 56 μm, 56 μm and 850 μm; an order of magnitude reduction in the radial direction compared with single-impulse focusing.

6.4.1 Transported cloud properties

For many experiments it is also important to consider changes to the velocity distribution and hence the collision rate and phase-space density. Unless the collision rate of a gas is sufficiently high, then Bose-Einstein condensation via sustainable evaporative cooling is impossible. Changes in the collision rate and phase-space density of the focused cloud are complicated by the fact that alternate-gradient lensing automatically leads to an anisotropic focused distribution both in space *and* in velocity.

At the $\mathcal{B}_{r,z} = 0$ focus of the cloud the $\mathcal{ABCD}_{r,z}$ matrix has radial and axial spatial widths $\sigma_r = \mathcal{A}_r\sigma_R$ and $\sigma_z = \mathcal{A}_z\sigma_R$ respectively. The radial and axial velocity widths are given by:

$$\sigma_{v_{r,z}} = \sqrt{k_B\mathcal{T}_{r,z}/m} = \sqrt{\mathcal{C}_{r,z}{}^2\sigma_R{}^2 + \sigma_V{}^2/\mathcal{A}_{r,z}{}^2}\,, \tag{6.2}$$

where $\mathcal{T}_{r,z}$ is the atomic cloud temperature. In the limit $\mathcal{C}_{r,z}\sigma_R \ll \sigma_V/\mathcal{A}_{r,z}$, the velocity width of the focused cloud is inversely proportional to its spatial width and $\sigma_{v_{r,z}} = \sigma_V/\mathcal{A}_{r,z}$. In Figure 6.15 phase-space plots of the AR and RA strategies from the rightmost points of Figures 6.14 (a) and (b) were generated with a 30,000 atom simulation. The effect of aberration is clearly seen when comparing the purely harmonic lenses (subscript H) and the Monte Carlo simulation with the full magnetic fields from realistic coils (subscript MC). The plots also demonstrate the inversely proportional relationship between spatial and velocity widths. Furthermore, in the Monte Carlo simulations there is much stronger correlation between position and velocity.

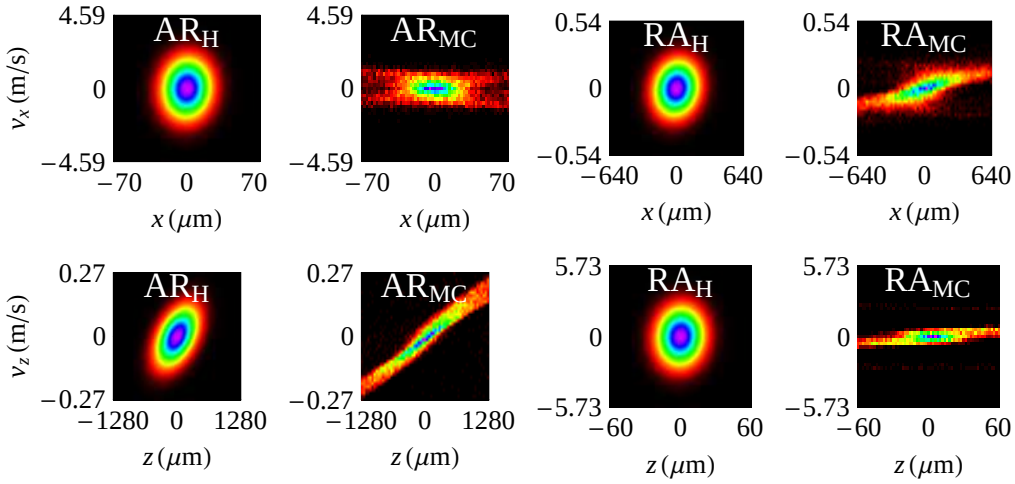

Figure 6.15: Phase-space plots of the AR and RA strategies from the rightmost points of Figures 6.14 (a) and (b) respectively. Both a harmonic lens calculation (subscript H) and a Monte Carlo simulation with the full magnetic fields from realistic coils (subscript MC) are plotted. In the $\mathrm{AR_{MC}}$ plot there are 45% $(x - v_x)$ and 42% $(z - v_z)$ of the initial 30,000 atoms present. In the $\mathrm{RA_{MC}}$ plot there are 61% $(x - v_x)$ and 24% $(z - v_z)$ of the atoms present. The effects of aberration are clearly seen when comparing the harmonic and realistic magnetic coils. [Figure generated in collaboration with A. S. Arnold.]

The anisotropic temperature in the focused cloud means that captured atoms in a cylindrically symmetric harmonic trap with radial and axial angular frequencies ω_r' and ω_z', will rethermalise to an isotropic temperature via elastic collisions. The prime is used to distinguish the trap frequencies from that of the lens. The total (potential+kinetic) energy of the focused cloud is equated with that of a 3D harmonic oscillator at equilibrium temperature $\mathcal{T}$ (i.e. $\frac{1}{2}k_B\mathcal{T}$ average energy per atom for each space and velocity dimension). The equilibrium temperature of the focused cloud after thermalisation is thus:

$$\mathcal{T} = \frac{m}{6k_B}\left(2\omega_r'^{\,2}{\sigma_r}^2 + \omega_z'^{\,2}{\sigma_z}^2 + 2{\sigma_{v_r}}^2 + {\sigma_{v_z}}^2\right). \tag{6.3}$$

In many experiments other physical properties of the atomic cloud are of interest: the atomic density $n \propto 1/({\sigma_r}^2\sigma_z)$, collision rate $\Gamma_{\rm el} \propto n\sqrt{\mathcal{T}}$ and phase-space density PSD $\propto n/(\mathcal{T}_r{\mathcal{T}_z}^{1/2})$. In order to minimise the loss of phase-space density during thermalisation of the focused cloud, it can be shown that it is best to choose ω_r' and ω_z' such that the potential energy is equal in all spatial dimensions and the total potential energy is equal to the total kinetic energy of the cloud [154]. The physical properties of the focused atomic clouds of Figure 6.15 are displayed in Table 6.3. The relative values for the density n, collision rate $\Gamma_{\rm el}$ and phase-space density can be converted into absolute values using typical initial experimental values: $\langle n\rangle = 10^{10}\,{\rm cm}^{-3}$ (an atom number $N = 3\times10^7$ in the unfocused cloud), $\Gamma_{\rm el} = 3\,{\rm s}^{-1}$ (see Appendix E) and phase-space density PSD=2×10^{-6}.

Note that the Monte Carlo relative density increases in Table 6.3 are lower than those in Figure 6.14 by a factor of ≈ 2, but the fraction of atoms in the focus are higher by a factor of ≈ 2. In Figure 6.14 the density is estimated by measuring the fraction of atoms arriving at the harmonic focus. Here, a 6-dimensional Gaussian phase-space fit to the narrow central peak of the bimodal focus was made to explicitly obtain σ_r, σ_z, $\mathcal{T}_r$ and $\mathcal{T}_z$. The fraction of atoms in this Gaussian focus was used for $\mathcal{F}$ here.

An interesting result of Table 6.3 is that the aberrations of 'real' lenses work to one's advantage, to some extent, in that the atoms can be loaded into a trap with a shallower depth than atoms focused by a purely harmonic lens, and phase-space density loss is reduced during rethermalisation. This is due to the

	t	$\mathcal{F}$	$\sigma_{r,z}(\mu\text{m})$	$\mathcal{T}_{r,z}(\mu\text{K})$	$\omega'_{r,z}/2\pi\,(\text{Hz})$	n	Γ_{el}	PSD
AR_{H}	0	1	400, 400	20, 20	*17.4, 17.4*	1	1	1
	T	1	15.2, 257	13900, 60.9	*12000, 47.3*	1080	23200	0.892
	T_R	1	15.2, 257	9260, 9260	9850, 584	1080	23200	0.108
AR_{MC}	0	1.000	400, 400	20, 20	*17.4, 17.4*	1	1	1
	T	0.308	23, 500	2720, 57	*3530, 23.5*	74.5	713	0.325
	T_R	0.308	23, 500	1830, 1830	2900, 133	74.5	713	0.085
RA_{H}	0	1	400, 400	20, 20	*17.4, 17.4*	1	1	1
	T	1	128, 12.2	197, 21600	*170, 18700*	319	6110	0.988
	T_R	1	128, 12.2	7320, 7320	1040, 10900	319	6110	0.046
RA_{MC}	0	1.000	400, 400	20, 20	*17.4, 17.4*	1	1	1
	T	0.305	200, 20	105, 1670	*79.7, 3180*	24.4	137	0.509
	T_R	0.305	200, 20	627, 627	195, 1950	24.4	137	0.139

Table 6.3: Physical properties of the two different alternate-gradient strategies modelled, AR and RA from the rightmost points in Figs. 6.14 (a) and (b) respectively. Subscripts H and MC respectively denote a simulation with purely harmonic lenses and a Monte Carlo simulation with the full magnetic fields from realistic lens coils. The measured parameters are: fraction of atoms in the Gaussian focus $\mathcal{F}$ (see text), radial/axial cloud radius $\sigma_{r,z}$, radial/axial temperature $\mathcal{T}_{r,z}$, radial/axial trap frequency $\omega'_{r,z}$, relative density n, relative collision rate Γ_{el} and relative phase space density PSD. The effective trap frequencies for the initial ($t = 0$) and focused ($t = T$) cloud (italicised) are equilibrium values based on $\omega' = \frac{1}{\sigma}\sqrt{k_B\mathcal{T}/m} = \sigma_v/\sigma$. The actual frequencies of the trap the atoms are loaded into at $t = T$ are denoted in the $t = T_R$ lines (the cloud properties after T plus the thermalisation time).

reduced anisotropy of the spatial and velocity distributions at the focus. The focused atoms have a relatively high temperature and one needs a trap depth of $\approx 10\,\text{mK}$ to trap the focused atoms.

If the trap that is being loaded is harmonic, with a large capture volume, then the rms size of the cloud will be linked to the equilibrium temperature after elastic collisions rethermalise the initially bimodal image distribution. In order to keep the high density core of the atomic cloud, the high energy atoms must be removed on a time scale that is rapid compared to rethermalisation - this could be achieved with strong RF evaporative cooling or by shining resonant dark SPOT beams [160] at the focal region. A trap with a small capture volume, e.g. an atom chip [110, 111] or a focused optical dipole beam trap [87], is ideal as only the high density core of atoms will be captured in the trap.

Chapter 6 summary

- A Strategy I lens can be used to focus an atomic cloud in the radial direction. Aberrations are reduced by increasing the size of lens. There is a marked difference in performance when comparing real coils with their parabolic approximations and the predictions made using $\mathcal{ABCD}$-matrices.
- The optimised double coil lenses (Strategies II and III) out perform the single coil lens.
- The only viable strategy for producing single-impulse isotropic 3D focusing is the baseball lens (Strategy VI).
- The combination of a laser guide and magnetic lenses makes a good transport scheme. The lack of losses from the axial-only lens (Strategy IV) is outweighed by the convenience and better harmonicity of the axial focusing/radial defocusing lenses (Strategies II and III). Pulse losses from the latter are 2% for the lenses simulated.
- The alternate-gradient method to focus an atomic cloud produces a highly focused core making it an ideal method for loading microtraps. The rethermalisation temperature and phase space density changes for harmonic trap loading were calculated.